Accurate Modeling of Dual Dipole and Slot Elements Used with Photomixers for Coherent Terahertz Output Power

Sean M. Duffy, *Member, IEEE*, S. Verghese, *Member, IEEE*, K. A. McIntosh, Andrew Jackson, A. C. Gossard, and S. Matsuura

Abstract—Accurate circuit models derived from electromagnetic simulations have been used to fabricate photomixer sources with optimized high-impedance antennas. Output powers on the order of 1 μW were measured for various designs spanning 0.6–2.7 THz. The improvement in output power ranged from 3 to 10 dB over more conventionally designed photomixers using broad-band log-spiral antennas. Measured data on single dipoles, twin dipoles, and twin slots are in good agreement with the characteristics predicted by the design simulations.

Index Terms—Equivalent circuits, modeling, photoconducting devices, submillimeter-wave antennas, submillimeter-wave mixers.

I. INTRODUCTION

PHOTOCONDUCTIVE switches are voltage-biased photoconductors, such as low-temperature-grown (LTG) gallium arsenide (GaAs), widely used to generate terahertz transients by excitation with subpicosecond laser pulses. Photomixers are continuous-wave (CW) versions of the photoconductive switch that produce the difference frequency of a pair of CW detuned laser diodes [1], [2]. CW applications for photomixers include high-resolution molecular spectroscopy [3]–[5] and local oscillators for terahertz heterodyne detectors [6], [7]. Compared to modern varactor multipliers, photomixers have much greater tuning bandwidth, but also emit lower output power [8], [9]. Optimizing a design for output power involves a careful tradeoff between the thermal design, optical coupling, circuit design, and antenna design [2]. This paper describes a detailed RF analysis of a family of high-output-power photomixers and develops equivalent circuits that other practitioners can use for optimization to particular applications.

The planar metallization of the photoconductive switch is easily integrated with planar antennas. By mounting the LTG GaAs to a silicon substrate lens, the radiation is focused into Gaussian beam optics [10]. Using this configuration, the basic design and modeling approach for the planar circuitry utilizes commercially available electromagnetic (EM) simulators and develops equivalent-circuit models when necessary. Modern EM simulators using moment methods and finite-element methods are fast, accurate, and available. As a first design example, a 630-GHz full-wavelength dipole is described that demonstrates some of the tradeoffs involved in designing a photomixer source. This design is relatively straightforward to simulate since well-defined ports are available to the EM simulator that enable calculation of the antenna impedance as viewed by the photoconductor. Higher output powers are available from more sophisticated designs that are subsequently described. These designs use dual-antenna elements such as dipoles and slots [11]–[16], due to an improved beam pattern, an improved impedance match, and the more favorable terminal characteristics of antennas that have the photoconductor electrodes located away from the antenna drive point. Their geometries, however, lack convenient port descriptions for the EM simulators to model the embedding impedance. Therefore, equivalent-circuit models based on EM calculations are used to provide a port definition that is practical and accurate. Dual-dipole designs were fabricated and measured during operation at 0.85, 1.0, 1.6, and 2.7 THz. A 1.4-THz dual-slot design was also fabricated and measured. The measured output power levels and operating frequencies reported for these photomixers represent state-of-the-art results.

II. SINGLE-DIPOLE PHOTOMIXER FOR 630 GHz

A. Design and Performance

All of the photomixers discussed here were fabricated from LTG–GaAs layers with thicknesses 0.2–1.5 μm deposited by molecular-beam epitaxy on 3-in semiinsulating GaAs substrates. The photocarrier lifetime was typically between 200–300 fs, as measured by pump–probe reflectivity near the wavelength 850 nm. Electron-beam lithography and a liftoff process are used to define the Ti : Au electrodes and terahertz structures. As an example, Fig. 1 shows operating characteristics as well as a scanning-electron micrograph (SEM) of a 630-GHz photomixer. The 8×6 μm LTG–GaAs switch contains four 0.2-μm-wide electrodes separated by 1.8-μm gaps. The switch was biased with a dc voltage and was modulated by the optical beating of the combined output of two detuned laser diodes operating near the wavelength $\lambda = 850$ nm [17]. The
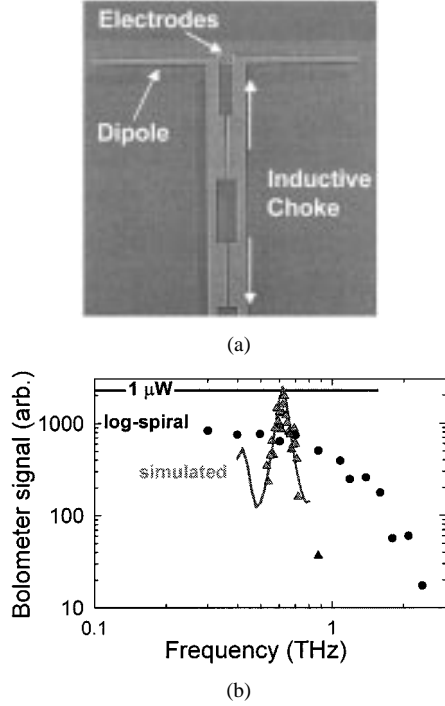
(a)

(b)

Fig. 1. (a) SEM photograph of full-wave dipole photomixer. (b) Measured (triangles) and calculated (solid line) results of full-wave dipole. Also shown are log-spiral measurements (circles).

Fig. 2. (a) Equivalent-circuit model for photomixer constructed of full-wave dipole. (b) Calculated impedance at photoconductor $[i(\omega), G]$: the choke impedance (solid squares), antenna with electrodes (solid diamonds), and total input impedance (solid circles).

antenna radiates into the GaAs substrate ($\varepsilon_{\mathrm{r}} = 12.9$) attached to a high-resistivity Si lens partially collimating the beam [10], [18].

When illuminated, the switch can be modeled in the small-signal limit as a current source with an output conductance of approximately $I_{\mathrm{dc}}/V_{\mathrm{dc}}$ and an output susceptance that is dominated by parasitic capacitance from the fringing fields between the 0.2-μm-wide fingers [18], [19]. Fig. 2 shows a small-signal equivalent circuit for the photomixer attached to its antenna and dc-bias lines. The design goal is to maximize the power transfer from the photomixer to the antenna. The terahertz conductance of the photomixer is low—typically $< (10 \text{ k}\Omega)^{-1}$ [18]—and conjugate impedance matching is, therefore, problematic. Consequently, the output power is proportional to the antenna resistance presented to the photomixer and designs with larger resistances will provide higher output powers.

There is some flexibility in the design of the interdigitated electrodes, within the three constraints of minimizing the parasitic capacitance, keeping the structure electrically small, and maintaining efficient optical coupling to the focused laser beams at $\lambda = 850$ nm. The bias lines for the design shown in Fig. 1 include a terahertz choke that presents a negative shunt susceptance (inductive) that cancels the parasitic capacitance at the design frequency. In addition, a high-impedance full-wave dipole was used to provide greater than a 3-dB improvement in the impedance match, compared to a frequency-independent spiral antenna.

The process of obtaining an optimum impedance match relies on accurate predictions of the terahertz impedance of the
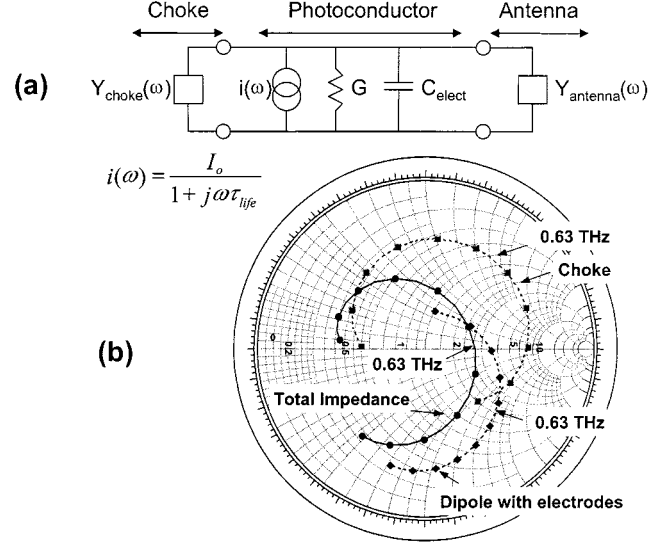
various elements depicted in Fig. 1. The input impedance of a full-wave dipole was calculated with the interdigitated electrodes at the drive point. The excitation source was a coplanar-strip (CPS) mode that is a standard calibrated port available from our commercial method-of-moments simulator.[1][2] Fig. 2 shows the embedding impedance seen by the photoconductor, where the photoconductor now comprises a notional current source in shunt connection with the real photoconductance G. Terahertz leakage down the bias lines is minimized by presenting a high impedance at the antenna terminals using a choke made with alternating quarter-wave sections of high- and low-impedance CPS lines. In this design, the first section of the high-impedance line near the antenna is operated less than a quarter-wavelength and presents an inductive susceptance that tunes out the capacitance from the photomixer. Fig. 2 shows the choke impedance. To a good approximation, the individual elements whose S-parameters were calculated with the EM simulator can then be connected together in a simple circuit simulator to predict the total embedding impedance, which is also shown in Fig. 2. The resonant resistance of the dipole with the photomixer and choke is 174 Ω. A comparison of the ratio of resistance of dipole to spiral (71 Ω) in Fig. 1 shows the measured 2.45 times improvement in output power [6].

III. DUAL-DIPOLE ELEMENTS

Dual antenna elements possess several advantages over single antenna element designs. These include more symmetric beam patterns, leading to higher Gaussian beam efficiency [14] and higher radiating resistance. The SEM photograph of a dual-dipole design shown in Fig. 3 uses an electrode region centered between two dipoles and connected via CPS transmission lines whose lengths are chosen to resonantly tune out the electrode

---

[1]Agilent Momentum, HPEEsof, Santa Cruz, CA.

[2]Frequency limitations in Agilent Momentum required a $10\times$ scaling in dimensions. The following calculated results have been scaled accordingly.
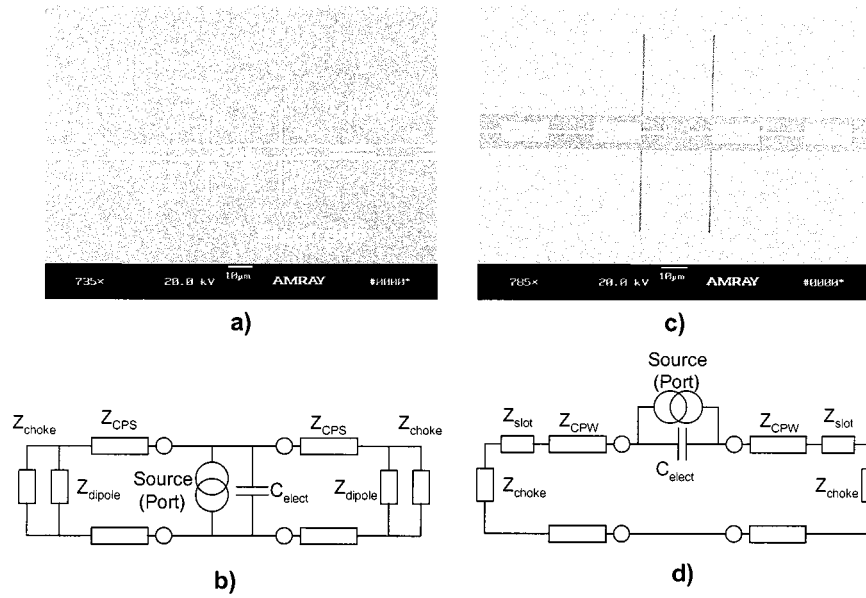
Fig. 3.   (a) SEM photograph of dual dipole (1.6-THz design). (b) Equivalent-circuit model for dual dipole. (c) SEM photograph of dual slot (1.4-THz design). (d) Equivalent-circuit model for dual slot.

capacitance. However, the primary advantage of the dual dipole is the ease in design of the photomixer for high-frequency operation.

The behavior of the dual dipole is illustrated by the equivalent-circuit model in Fig. 3. The choke and dipoles are connected in a parallel connection to the electrode capacitance and photoconductance. Therefore, the admittance at the photoconductor is $Y_{\text{trans}} = 2G_{\text{trans}} + j2B_{\text{trans}}$, where G_{trans} and B_{trans} are the conductance and susceptance, respectively, of a single dipole transformed through the CPS transmission line. Therefore, the following two important characteristics are displayed: 1) the input resonant resistance is reduced in half compared to a single dipole arm and 2) only half of the inductive tuning needs to come from each dipole arm. Therefore, the maximum attainable resistance from a dual dipole is limited. However, the reduced amount of required tuning of the dual dipoles allows operation at higher frequencies with examples up to 2.7 THz shown later in this work. Also, electrode structures with many closely spaced fingers may be used. While these structures possess higher capacitance, they can also handle larger photocurrents leading to higher terahertz power [20].

The problem in applying the equivalent-circuit model of Fig. 3 is finding accurate and meaningful port definitions for use with EM simulators. Therefore, the electrodes are solved using an EM simulator and then converted to a lumped-circuit model. The antenna, CPS transmission line, and choke are also calculated using the EM simulator and then combined in a circuit simulation using the drive port across the photoconductor capacitance as above.

A. Electrode Capacitance with CPS Feed

A convenient transmission line for dual dipoles uses CPSs, as shown in Fig. 3. The CPS acts as an impedance transformer connecting the photomixer to the dipole antennas and provides dc

bias to the photomixer region with the bias contact pads placed away from the antenna near the edge of the substrate.

The interdigitated electrode region possesses a capacitance solved using either a conformal-mapping solution [21] or a full-wave EM simulation converted into a lumped-circuit model. However, the electrode also possesses a length of transmission line related to the physical length. The equivalent-circuit model and layout of the electrode region is shown in Fig. 4. The layout of the electrode region can be solved using an EM simulator and the equivalent lumped-element capacitance found from

$$C_{\text{elect}} = \frac{2j S_{11}^{\text{EM}} e^{j\beta L_{\text{elect}}}}{\omega Z_{\text{cps}}(1 + S_{11}^{\text{EM}} e^{j\beta L_{\text{elect}}})}. \tag{1}$$

where S_{11}^{EM} is found from the EM simulator result, β is the propagation constant using $\varepsilon_{\text{eff}} = (\varepsilon_{\text{r}} + 1)/2$ ($\varepsilon_{\text{eff}} = 6.9$), L_{elect} is the physical length, and Z_{cps} is the characteristic impedance of the CPS line. For example, for eight 0.24-μm fingers with 0.76-μm separation in a 7×5 μm area with 1-μm-wide lines and 6-μm center–center spacing, $Z_{\text{cps}} = 146$ Ω, $L_{\text{elect}} = 9.2$ μm, and $S_{11}^{\text{EM}} = (-0.324, -0.237)$ at 1 THz, and the capacitance is $C_{\text{elect}} = 0.96 + j0.02$ fF. The imaginary part of (1) provides a check of the validity of the lumped-element approximation. The ratio of the imaginary to real part of (1) for this electrode is 0.02 at 1 THz and 0.22 at 2 THz.

The accuracy of the circuit model compared to an EM simulation over a 0.2–2-THz band is demonstrated in Fig. 4. It is noticed that the single lumped capacitor approximation begins to break down as the electrode region exceeds 0.1 λ_{e}, where $\lambda_{\text{e}} = \lambda_{\text{o}}/\sqrt{\varepsilon_{\text{eff}}}$. Additional lumped capacitances must be included for accurate predictions of the finger geometry at higher frequencies. A three-capacitor model, shown in Fig. 4, is used for higher frequency designs. A potential problem of applying this circuit model is the assumption that the outer fingers do not generate any photocurrent.
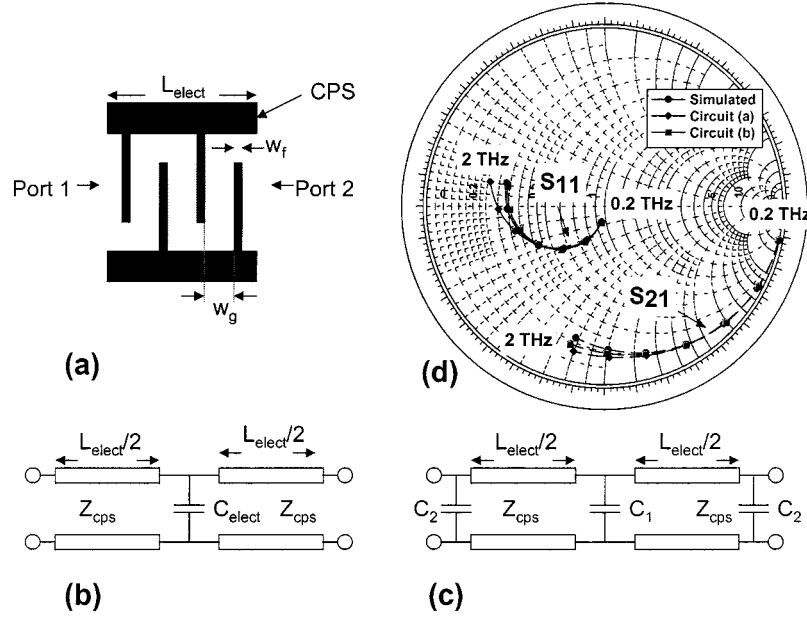
Fig. 4. (a) Equivalent-circuit model for electrode (low-frequency model): $C_{\text{elect}} = 0.92$ fF, $Z_{\text{cps}} = 145\ \Omega$, and $L_{\text{elect}} = 9.2\ \mu$m. (b) Equivalent-circuit model for electrode (high-frequency model): $C_1 = 0.78$ fF and $C_2 = 0.14$ fF. (c) Calculated results using EM simulator and circuit models for 0.2–2 THz shown in 145-Ω Smith chart.

B. Conductor Details

The metal thickness of the electrodes causes additional capacitance for the electrode region beyond the infinitely thin metal assumed in the above calculations. The metal has cross-sectional dimensions of 0.2-μm width and 0.15-μm height. Results from HFSS[3] calculations and measurements demonstrate that the 0.2-μm-wide and 0.15-μm-high finger can be modeled as a zero-height finger of 0.23–0.24-μm width. Calculated results in the designs of this work use a width of 0.24 μm for this reason. The first iteration of designs without this correction was off slightly in frequency due to this effect.

The peak operating frequency of dual-dipole and dual-slot designs have been successfully analyzed and designed without considering the effects of loss. However, for accurate power-level comparisons, the loss must be included. For the CPS dimensions used in this work, i.e., linewidths of 1- and 6-μm center–center separation, conductor loss is found to be dominant over dielectric and radiative losses [22]. An adjustment to the loss has been added through the metal conductivity since dc measurements indicate that the thin-film conductivity is 2.0×10^7 S/m. Thin films typically have conductivities lower than the bulk result and may be partly due to the lower conductivity of the Ti adhesion layer.

Radiation efficiency is normally defined as the ratio of the radiated power to input power [23]. As a measure of the effect of the finite conductivity of the conductors, a conductor radiation efficiency is defined as the ratio of the resonant resistance of the dual dipoles at the photoconductor electrodes calculated with loss to the resonant resistance calculated assuming a perfect electric conductor. This is valid since, at the reference plane of the photoconductor electrodes (quarter-wavelength from a half-wave dipole), the loss can be modeled near resonance as
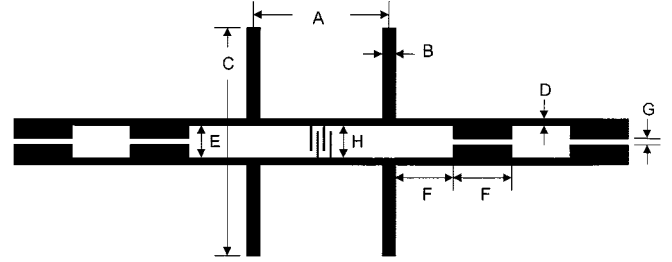
Fig. 5. Geometry of dual-dipole designs with parameters given in Table I.

TABLE I
DIMENSIONS FOR DIPOLE DESIGNS IN MICROMETERS

Name	A	B	C	D	E	F	G	H	N_f	w_f	w_g
D1	55.4	2.5	68.4	1.0	5.0	33.7	1.0	5.0	8	0.2	0.8
D2	46.7	2.5	54.6	1.0	5.0	27.7	1.0	5.0	8	0.2	0.8
D3	28.8	1.5	34.3	1.0	5.0	17.9	1.0	5.0	8	0.2	0.8
D4	20.0	1.0	20.7	1.0	4.0	10.6	1.0	4.0	6	0.2	0.8
S1									8	0.2	0.8

a shunt resistor. Dual-dipole designs for 0.85, 1.05, 1.60, and 2.70 THz, discussed in the following section, have radiation efficiencies of 72%, 67%, 64%, and 60%, respectively, defined in this way. However, leakage through the choke, reduced power due to mutual coupling, and losses to Gaussian beam coupling are not included in this measure. Nevertheless, it does demonstrate that the metal of the photomixer operating at room temperature still provides reasonably efficient coupling into the hyperhemisphere at these frequencies.

C. Designs and Results

A number of dual-dipole designs have been fabricated in the 0.85–2.7-THz range. Several of these designs illustrated in Fig. 5 with dimensions given in Table I are compared with modeled predictions. Their terahertz output characteristics were
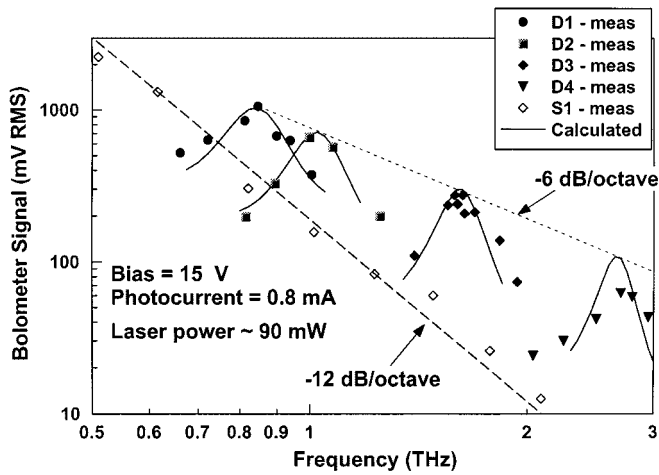
Fig. 6. Results from a bolometer for dual dipoles $D1$, $D2$, $D3$, $D4$, and spiral $S1$. Calculated results are shown in solid lines. The -6-dB/octave curve demonstrates the predicted dipole rolloff and the -12-dB/octave curve demonstrates the predicted spiral rolloff.

TABLE II
CALCULATED PREDICTIONS OF PHOTOMIXER DESIGNS

Name	Frequency (THz)	Radiation efficiency (%)	Dipole resistance (Ω)	Spiral load resistance (Ω)	Dipole/spiral (dB)
D1	0.85	72	217	58	5.7
D2	1.05	67	214	53	6.0
D3	1.6	64	203	39	7.2
D4	2.7	60	217	21	10.1

measured as described above [24]. Fig. 6 shows the measured and calculated results. The calculated results are obtained by taking a ratio of dipole to spiral resistance. For identical electrode structures, this eliminates the effect of thermal heating, carrier lifetime, and coupling losses to the Gaussian beam optics. The calculated characteristics are also tabulated in Table II. The basic dual-dipole design uses half-wavelength dipoles spaced half-wavelength apart (minus the length to tune out the electrode capacitance). This basic design is used for $D1$, $D2$, $D3$, and $D4$ for operation at 0.85-, 1.05-, 1.6-, and 2.7-THz operation, respectively. The 2.7-THz design has measured values lower than predicted, as demonstrated in Fig. 6. Two reasons may account for this. The first is $D4$ has a smaller electrode region than the other designs, possibly allowing more spillover from the optical fiber. Secondly, additional terahertz power may have been lost due to substrate absorption in GaAs. The absorption was measured in the 1–4-THz range and leads to approximately 28% loss at 2.7 THz [25], [26].

The measured results using a spiral antenna with electrode geometry of 8×8 μm with eight fingers are also shown in Fig. 6. Measured power levels are obtainable to 2 THz before noise degrades the accuracy. From the equivalent-circuit model of Fig. 2, the output power from a photomixer is $P_\omega = 1/2 |i(\omega)|^2 \text{Re}(Z_{\text{load}})$, where Z_{load} includes the antenna impedance and the electrode capacitance. Since the spiral and electrode are connected in a parallel configuration, the power radiated is proportional to $\text{Re}(Z_{\text{load}}) = R_{\text{spiral}}/[1 + (\omega R_{\text{spiral}} C_{\text{elect}})^2]$. This shows that the load resistance seen by the current source decreases with frequency even though the spiral resistance remains 71 Ω. Essentially, the electrode capacitance "shorts out" the antenna resistance at high frequencies. Therefore, the resistance seen by the current source for a spiral antenna decreases by 6 dB/octave. As the terahertz current $i(\omega)$ shows, there is also a 6-dB/octave reduction to the terahertz photocurrent due to the lifetime of the carriers. However, the lifetime has an electric-field dependence that increases the effective lifetime of the carriers to approximately 1 ps for these photomixers [27], [28] making

the rolloff begin well below 1 THz. Therefore, the output power from spiral antennas drops by 12 dB/octave, as shown in the curve of Fig. 6.

The advantage of using resonant antennas for high-output-power photomixers is clear since two benefits arise. First, the radiation resistance is higher than frequency-independent designs due to the tradeoff of bandwidth. Second, the rolloff in output power is only caused by the lifetime of the carriers since the inductive tuning eliminates the rolloff due to the electrode capacitance. The output power behavior of the dual dipoles in Fig. 6 demonstrates the predicted 6-dB/octave rolloff. Therefore, for operation at frequencies above 1 THz, the improved high-output-power behavior of resonantly tuned antennas becomes more pronounced. The improvement in output power of 6–10 dB for the dual dipoles over the spiral is annotated in Table II. The corresponding output powers of $D1$, $D2$, $D3$, and $D4$ on our best material are 3, 2, 0.8, and 0.2 μW, respectively [24], and represent state-of-the-art photomixer results.

IV. DUAL-SLOT ELEMENTS

The dual slot is illustrated in the SEM photograph shown in Fig. 3. A coplanar waveguide (CPW) is used as the connecting transmission line and bias is applied across the electrodes. The primary advantage of the dual slot is the very high-output power that can be attained. Additionally, the Gaussian beam efficiency is increased over a single-slot element due to the reduced beamwidth in the E-plane. However, dual slots are best suited to low-frequency designs because it is more difficult to tune out the electrode capacitance than with the dual dipole.

The behavior is illustrated in the equivalent-circuit model of Fig. 3. The slots are connected in series, making the input impedance twice a single-slot arm $Y_{\text{slot}} = G_{\text{trans}}/2 + jB_{\text{trans}}/2$. Therefore, twice the resistance is attained from a dual-slot versus a single-slot arm and four times as much as the dipoles. This creates the possibility for very high resistance (and, therefore, very high-output powers) presented to the photoconductor. However, the inductive tuning is halved, making the need for each slot arm to present twice as much susceptance as a single-slot arm and four times as much as the dipole arms. This limits the useful operating frequencies to below 1 THz for these electrode geometries. A 1.4-THz design was constructed, but the increase in output power over an equivalent spiral design is less than the dipole designs presented above.

A. Electrode Capacitance for CPW Feed

An equivalent-circuit model for the electrodes in CPW is briefly described and shown in Fig. 7. The model considers the
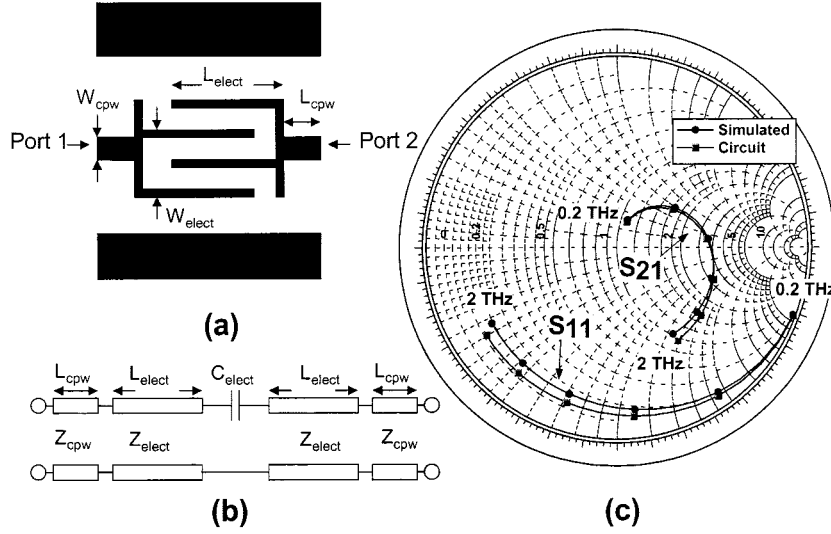
Fig. 7. (a) Layout of electrode geometry in CPW. (b) Equivalent-circuit model: $L_{\text{elect}} = 5.8\ \mu\text{m}$, $C_{\text{elect}} = 0.76$ fF, $Z_{\text{elect}} = 52\ \Omega$, $L_{\text{cpw}} = 1.1\ \mu\text{m}$, $W_{\text{cpw}} = 1.0\ \mu\text{m}$, and $Z_{\text{cpw}} = 80\ \Omega$. (c) Calculated results using EM simulator and circuit model for 0.2–2 THz shown in 80-Ω Smith chart.
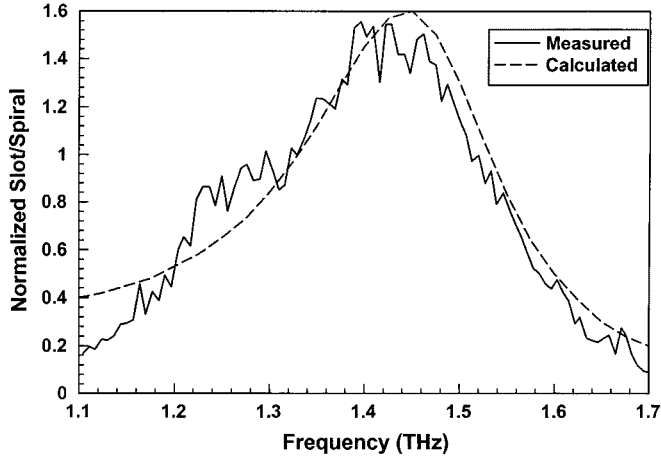

Fig. 8. Measured results from a bolometer for dual-slot design. Measured result is ratio of slot signal to spiral signal. Calculated result is ratio of calculated resistance of dual slot to spiral.

coplanar fingers to be sections of transmission lines with a series capacitance. Since currents in the center strip of CPW are concentrated at the outer edges of the strip, the effective linewidth of the center conductor is the outer finger-to-finger distance W_{elect}, as shown in Fig. 7. The length of the transmission line is the total finger length L_{elect} and, therefore, the lengths of the two transmission-line section overlap. The method finds the series capacitance using a CPW center linewidth (W_{cpw}) equal to the electrode–electrode width (W_{elect}). The capacitance is found by assuming a series element and using the EM calculation

$$C_{\text{elect}} = \frac{S_{21}^{\text{EM}} e^{2j\beta(L_{\text{elect}} + L_{\text{cpw}})}}{j2\omega Z_{\text{elect}}\left[1 - S_{21}^{\text{EM}} e^{2j\beta(L_{\text{elect}} + L_{\text{cpw}})}\right]}. \quad (2)$$

Here, W_{elect} is 4.24 μm and L_{elect} is 6.0 μm for the $8 \times 6\ \mu$m region with four 0.24-μm fingers with 6-μm lengths and 1.76-μm separation and ground–ground spacing of 13.0 μm.

Finally, the electrode region is connected with a high-impedance section of CPW with center strip width of 1.0 μm (80 Ω) that connects to the radiating slots. Including this discontinuity into the model and iterating slightly for better agreement ($L_{\text{cpw}} = 1.1\ \mu$m, $L_{\text{elect}} = 5.8\ \mu$m, and $C_{\text{elect}} = 0.76$ fF) with the EM simulation yields the results of 0.2–2.0 THz, as shown in Fig. 7.

B. Design Example and Results

As an example, the output power of the slot design in Fig. 3 is calculated and plotted versus the measured bolometer signal in Fig. 8. Dual full-wave slots are calculated to have an impedance at the photoconductor at 1.4 THz of $109 - j57\ \Omega$. A spiral antenna with identical electrode geometry is calculated to have a capacitance of 0.5 fF. Therefore, the impedance at 1.4 THz is $65.5 - j20.7\ \Omega$. The ratio of dual-slot resistance to spiral resistance is plotted in Fig. 8. The ratio eliminates the bolometer response and the water line at 1.41 THz [4]. Close agreement is again found for this modeling procedure.

V. Conclusion

This paper has presented a design method validated by measured terahertz results that allows accurate prediction of dipole and slot elements center fed by a photomixing source. The method combines the flexibility and speed of modern EM simulators with equivalent-circuit models that allows the integration of the photomixing current source and provides physical intuitive insight. The key to the modeling was developing accurate circuit models for the electrodes. Agreement between calculated and measured are good. Designs with state-of-the-art output powers from 0.6 to 2.7 THz were also measured.

References

[1] K. A. McIntosh, E. R. Brown, K. B. Nichols, O. B. McMahon, W. F. DiNatale, and T. M. Lyszczarz, "Terahertz photomixing with diode lasers in low-temperature-grown GaAs," *Appl. Phys. Lett.*, vol. 67, pp. 3844–3846, 1995.

[2] S. Verghese, K. A. McIntosh, and E. R. Brown, "Highly tunable fiber-coupled photomixers with coherent terahertz output power," *IEEE Trans. Microwave Theory Tech.*, vol. 45, pp. 1301–1309, Aug. 1997.

[3] A. S. Pine, R. D. Suenram, E. R. Brown, and K. A. McIntosh, "A terahertz photomixing spectrometer: Application to SO_2 self broadening," *J. Mol. Spectrosc.*, vol. 175, pp. 37–47, 1996.

[4] S. Verghese, K. A. McIntosh, E. K. Duerr, S. M. Duffy, L. J. Mahoney, and S. D. Calawa, "Terahertz spectroscopy of water vapor using a photomixer transceiver," in *Proc. IEEE 7th Int. Terahertz Electron. Conf.*, Nara, Japan, 1999, pp. 89–91.

[5] P. Chen, G. A. Blake, M. C. Gaidis, E. R. Brown, K. A. McIntosh, S. Y. Chou, M. I. Nathan, and F. Williamson, "Spectroscopic applications and frequency control of submillimeter-wave photomixing with distributed-Bragg-reflector diode lasers in low-temperature-grown GaAs," *App. Phys. Lett.*, vol. 71, pp. 1601–1602, 1997.

[6] S. Verghese, E. K. Duerr, K. A. McIntosh, S. M. Duffy, S. D. Calawa, C.-Y. E. Tong, R. Kimberk, and R. Blundell, "A photomixer local oscillator for a 630-GHz heterodyne receiver," *IEEE Microwave Guided Wave Lett.*, vol. 9, pp. 245–247, June 1999.

[7] E. K. Duerr, K. A. McIntosh, S. M. Duffy, S. D. Calawa, S. Verghese, C. Y. E. Tong, R. Kimberk, and R. Blundell, "Demonstration of a 630-GHz photomixer used as a local oscillator," in *IEEE MTT-S Int. Microwave Symp. Dig.*, Anaheim, CA, 1999, pp. 127–130.

[8] S. Verghese, K. A. McIntosh, and E. R. Brown, "Optical and terahertz power limits in low-temperature-grown GaAs photomixers," *Appl. Phys. Lett.*, vol. 71, pp. 2743–2745, 1997.

[9] S. Matsuura, G. A. Blake, R. A. Wyss, J. C. Pearson, C. Kadow, A. W. Jackson, and A. C. Goddard, "Free-space traveling-wave THz photomixers," in *Proc. IEEE 7th Int. Terahertz Electron. Conf.*, Nara, Japan, 1999, pp. 24–27.

[10] D. B. Rutledge and M. S. Muha, "Imaging antenna arrays," *IEEE Trans. Antennas Propagat.*, vol. AP-30, pp. 535–540, July 1982.

[11] G. M. Rebeiz, "Millimeter-wave and terahertz integrated circuit antennas," *Proc. IEEE*, vol. 80, pp. 1748–1770, Nov. 1992.

[12] P. T. Parrish, T. C. L. G. Sollner, R. H. Mathews, H. R. Fetterman, C. D. Parker, P. E. Tannenwald, and A. G. Cardiasmenos, "Printed dipole Schottky diode millimeter wave antenna array," *SPIE Millimeter Wave Technol.*, vol. 337, pp. 49–52, 1982.

[13] A. Skalare, Th. De Graauw, and H. van de Stadt, "A planar dipole array antenna with an elliptical lens," *Microwave Opt. Technol. Lett.*, vol. 4, no. 1, pp. 9–12, 1991.

[14] D. F. Filipovic, W. Y. Ali-Ahmad, and G. M. Rebeiz, "Millimeter-wave double-dipole antennas for high-gain integrated reflector illumination," *IEEE Trans. Microwave Theory Tech.*, vol. 40, pp. 962–967, May 1992.

[15] D. F. Filipovic, S. S. Gearhart, and G. M. Rebeiz, "Double-slot antennas on extended hemispherical and elliptical silicon dielectric lenses," *IEEE Trans. Microwave Theory Tech.*, vol. 41, pp. 1738–1749, Oct. 1993.

[16] M. Bin, M. C. Gaidis, J. Zmuidzinas, T. G. Phillips, and H. G. LeDuc, "Quasi-optical SIS mixers with normal metal tuning structures," *IEEE Trans. Appl. Superconduct.*, vol. 7, pp. 3584–3588, June 1997.

[17] J. S. Major, Jr, S. O'Brien, V. Vulgazov, D. F. Welch, and R. J. Lang, "High-power single-mode AlGaAs distributed Bragg reflector laser diodes operating at 856 nm," *Electron. Lett.*, vol. 30, pp. 496–497, 1994.

[18] E. R. Brown, F. W. Smith, and K. A. McIntosh, "Coherent millimeter-wave generation byheterodyne conversion in low-temperature-grown GaAs photo-conductors," *J. Appl. Phys.*, vol. 73, pp. 1480–1484, 1993.

[19] R. H. Kingston, *Detection of Optical and Infrared Radiation*. Berlin, Germany: Springer-Verlag, 1978.

[20] E. R. Brown, K. A. McIntosh, F. W. Smith, K. B. Nichols, M. J. Manfra, C. L. Dennis, and J. P. Mattia, "Milliwatt output levels and superquadratic bias dependence in a low-temperature-grown GaAs photomixer," *Appl. Phys. Lett.*, vol. 64, pp. 3311–3313, 1994.

[21] Y. C. Lim and R. A. Moore, "Properties of alternately charged coplanar parallel strips byconformal mappings," *IEEE Trans. Electron Devices*, vol. 15, pp. 173–180, Mar. 1968.

[22] K. C. Gupta, R. Garg, and R. Chadha, *Computer-Aided Design of Microwave Circuits*. Norwood, MA: Artech House, 1981.

[23] C. A. Balanis, *Antenna Theory: Analysis and Design*, 2 ed. New York: Wiley, 1997.

[24] A. W. Jackson, "Low-temperature-grown GaAs photomixers designed for increased terahertz output power," Ph.D. dissertation, Mater. Dept., Univ. California at Santa Barbara, Santa Barbara, CA, 1999.

[25] C. J. Johnson, G. H. Sherman, and R. Weil, "Far infrared measurement of the dielectric properties of GaAs and CdTe at 300 K and 8 K," *Appl. Opt.*, vol. 8, pp. 1667–1671, Aug. 1969.

[26] S. Matsuura, unpublished data.

[27] K. A. McIntosh, K. B. Nichols, S. Verghese, and E. R. Brown, "Investigation of ultrashort photocarrier relaxation times in low-temperature-grown GaAs," *Appl. Phys. Lett.*, vol. 70, pp. 354–356, 1997.

[28] N. Zamdmer, Q. Hu, K. A. McIntosh, and S. Verghese, "Increase in response time of low-temperature-grown GaAs photoconductive switches at high voltage bias," *Appl. Phys. Lett.*, vol. 75, pp. 2313–2315, 1999.

Sean M. Duffy (S'91–M'99), photograph and biography not available at time of publication.

S. Verghese (S'85–M'87), photograph and biography not available at time of publication.

K. A. McIntosh, photograph and biography not available at time of publication.

Andrew Jackson, photograph and biography not available at time of publication.

A. C. Gossard, photograph and biography not available at time of publication.

S. Matsuura, photograph and biography not available at time of publication.